Optimization of Nuclear Polarization in an Alkali-Noble Gas Comagnetometer

Emmanuel Klinger[1,2,*,†] Tianhao Liu[1,2] Mikhail Padniuk[3] Martin Engler[1,2]
Thomas Kornack[4] Szymon Pustelny[3] Derek F. Jackson Kimball[5]
Dmitry Budker[1,2,6] and Arne Wickenbrock[1,2]

[1] *Johannes Gutenberg-Universität Mainz, Mainz 55128, Germany*

[2] *Helmholtz-Institut Mainz, GSI Helmholtzzentrum für Schwerionenforschung, Mainz 55128, Germany*

[3] *Marian Smoluchowski Institute of Physics, Jagiellonian University in Krakow, Łojasiewicza 11, Krakow 30-348, Poland*

[4] *Twinleaf LLC, 300 Deer Creek Drive, Plainsboro, New Jersey 08536, USA*

[5] *Department of Physics, California State University – East Bay, Hayward, California 94542, USA*

[6] *Department of Physics, University of California, Berkeley, California 94720, USA*

Self-compensated comagnetometers, employing overlapping samples of spin-polarized alkali and noble gases (for example K-^{3}He) are promising sensors for exotic beyond-the-standard-model fields and high-precision metrology such as rotation sensing. When the comagnetometer operates in the so-called self-compensated regime, the effective field, originating from contact interactions between the alkali valence electrons and the noble-gas nuclei, is compensated with an applied magnetic field. When the comagnetometer begins operation in a given magnetic field, spin-exchange optical pumping establishes an equilibrium between the alkali electron-spin polarization and the nuclear-spin polarization. Subsequently, when the magnetic field is tuned to the compensation point, the spin polarization is brought out of the equilibrium conditions. This causes a practical issue for long measurement times. We report on a method for closed-loop control of the compensation field. This method allows optimization of the operating parameters, especially magnetic field gradients, in spite of the inherently slow (hours to days) dynamics of the system. With the optimization, higher stable nuclear polarization, longer relaxation times, and stronger electron-nuclear coupling are achieved which is useful for nuclear-spin-based quantum memory, spin amplifiers, and gyroscopes. The optimized sensor demonstrates a sensitivity comparable to the best previous comagnetometer but with four times lower noble-gas density. This paves the way for applications in both fundamental and applied science.

I. INTRODUCTION

Over the past 20 years, vapor-cell-based atomic sensors [1] have received growing attention due to the possibilities of miniaturization and low power consumption [2], features which compare favorably to cryogenically cooled sensors such as superconducting interferometers .

In a gas containing alkali atoms and polarized noble-gas atoms, the electrons of the alkalis feel an effective magnetic field resulting from contact interactions between the electrons and the noble-gas nuclei. An applied external magnetic field can be tuned to cancel this effective field, then such a comagnetometer operates at the so-called compensation point. Under these conditions, the polarized noble-gas nuclei can adiabatically follow a slowly changing magnetic field. This renders the device insensitive to transverse magnetic fields that vary more slowly than the response time of the system, typically, several hundreds of milliseconds [3]. Another advantage of operating near the compensation field is that the alkali vapor may be brought into the spin-exchange-relaxation-free (SERF) regime [4] if the frequency of the alkali-spin Larmor precession is much lower than the rate of spin-exchange collisions. Operation in the SERF regime significantly improves the sensitivity of the comagnetometer [5] to nonmagnetic perturbations.

While designed to be insensitive to magnetic fields, self-compensated comagnetometers are exquisitely sensitive to nonmagnetic interactions. In the self-compensation regime the noble-gas magnetization follows changes in the low-frequency external magnetic field, which protects the alkali-metal polarization from the magnetic field perturbation [3,6]. However, this protection does not

---

*emmanuel.klinger@femto-st.fr

†Present address: Université de Franche-Comté, SupMicroTech-ENSMM, UMR 6174 CNRS, Institut FEMTO-ST, 25000 Besançon, France.

extend to nonmagnetic perturbations (e.g., rotation or exotic spin couplings), allowing the measurement of such perturbations. First demonstrated in the early 2000s [3], these devices were extensively improved in follow-up studies. It was shown that the effects of light shifts and radiation trapping can be minimized if the probed alkali species is polarized by spin-exchange optical pumping (hybrid pumping) [7]. Recently, the response of the system to a low-frequency field modulation was explored [8], which can be used for *in-situ* characterization of the comagnetometer at the compensation point. Noble-gas comagnetometers have proven to be sensitive gyroscopes [9–13] and powerful tools for exotic physics searches [6,13–16]. Due to the long coherence time of noble-gas spins and the ability to optically manipulate alkali-atom spins, comagnetometers have found applications in quantum memory assisted by spin exchange [17–19].

Although extremely sensitive, self-compensated comagnetometers are often difficult to operate for a long period of time (days) because of the need of frequent field zeroing, alignment of laser beams, etc. One way to improve the stability of the system is to use a high noble-gas pressure (for example 12 amg was used in Ref. [14], where $1\ \mathrm{amg} = 2.69 \times 10^{19}\ \mathrm{cm}^{-3}$). Although this approach is applicable for individual experiments, it poses challenges of producing and handling multiple gas-containing vapor cells at larger scales and thus acts as a bottleneck for wide usability in applications.

Here, we report on a method for following, in real time, the buildup of nuclear magnetization through spin-exchange optical pumping. This enables stationary working conditions to be reached, where the effective magnetic field experienced by alkali atoms is approximately zero. A ^{3}He-^{39}K-^{87}Rb comagnetometer is successfully operated at equilibrium nuclear polarization above 100 nT with a cell pressure below 3 amg [20] without frequent field zeroing. This is enabled by precise compensation of the field gradients inside the magnetic shield. In Sec. II, we review the effect of magnetic field gradients on the comagnetometer, showing that for a given cell, equilibrium nuclear magnetization can only be achieved at high pressure or low field gradients. In Sec. III, we present the experimental setup and show the measured effect of field gradients on the transverse and longitudinal relaxation rates and the evolution of nuclear magnetization over time. Polarization dynamics is further discussed in Sec. IV, and conclusions are drawn in Sec. V.

II. COMAGNETOMETER THEORY

We are interested in understanding how field gradients affect the equilibrium nuclear magnetization. Consider an ensemble of polarized electronic (^{39}K) and nuclear (^{3}He) spins enclosed in a perfectly spherical cell. The dynamics of the longitudinal component (along the light propagation direction, z) of the nuclear polarization follows [3]

$$\frac{d}{dt}P^n(t) = R_{\mathrm{se}}^{\mathrm{ne}}(P^e - P^n) - \frac{1}{T_1^n}P^n, \tag{1}$$

where $P^n(t)$ is the time-dependent fractional ^{3}He polarization, for which the steady-state value is determined as

$$P^n(t \to \infty) = \frac{R_{\mathrm{se}}^{\mathrm{ne}}}{1/T_1^n + R_{\mathrm{se}}^{\mathrm{ne}}}P^e. \tag{2}$$

Here P^e is the electronic spin polarization (in typical high sensitivity experiments, $P^e \approx 50\%$ [21]), $R_{\mathrm{se}}^{\mathrm{ne}} = \mathcal{N}_e \sigma_{\mathrm{se}}^{\mathrm{ne}} v$ is the spin-exchange rate for a noble-gas atom, $\sigma_{\mathrm{se}}^{\mathrm{ne}}$ is the spin-exchange cross-section, v is the characteristic relative velocity in alkali-noble gas collisions, $\mathcal{N}_e$ is the concentration of alkali atoms, and T_1^n is the longitudinal relaxation rate of nuclear spins.

The main contribution to the relaxation time T_1^n in many experiments comes from magnetic field inhomogeneities throughout the cell. In this case and for sufficiently high pressures [22,23],

$$\frac{1}{T_1^n} = D_n \frac{|\nabla B_\perp|^2}{B_z^2}, \tag{3}$$

where B_z is the leading field seen by the nuclear spins, and the transverse field gradients are characterized by $|\nabla B_\perp|^2 = |\nabla B_x|^2 + |\nabla B_y|^2$. There are various contributions to the field gradient, including the residual gradients from the magnetic shields, the field coils, as well as gradients due to the polarized spins (in our case dominated by nuclear spins). Note that the gradient due to polarized spins only occurs when the cell is not spherical. This gradient is proportional to $P^n \mathcal{N}_n$ and cannot be fully compensated by first-order gradient coils. Here we describe this effect using a phenomenological factor α, accounting for the asphericity of the cell, making the overall gradient

$$|\nabla B_\perp|^2 = |\nabla B_{\perp,0}|^2 + |\alpha P^n \mathcal{N}_n|^2, \tag{4}$$

with $|\nabla B_{\perp,0}|^2$ representing the first-order gradient that can be zeroed by gradient coils.

The noble-gas self-diffusion coefficient D_n is a function of the temperature Θ and the noble-gas density $\mathcal{N}_n$. It can be approximated by

$$D_n = D_0 \frac{\sqrt{\Theta/273\,\mathrm{K}}}{\mathcal{N}_n/1\,\mathrm{amg}}. \tag{5}$$

For $D_0 = 1.65\ \mathrm{cm}^2/\mathrm{s}$ in the case of ^{3}He [24], $\Theta = 458$ K (185 °C), and $\mathcal{N}_n \approx 3$ amg, the self-diffusion coefficient is roughly 0.71 cm^2/s.

A. Compensation point

In the comagnetometer, the principal mechanism via which nuclear and electronic spins couple to each other is spin-exchange collisions. Under particular conditions it turns out that this coupling can result in a suppression of sensitivity to slowly changing transverse magnetic fields. This suppression is maximal when the applied longitudinal magnetic field is tuned to the so-called compensation point B_c, where the coupling of nuclear and electronic spins is the strongest [3]:

$$B_c = -B_n - B_e = -\lambda M_n P^n - \lambda M_e P^e. \qquad (6)$$

Here $\lambda = 2\kappa_0 \mu_0 / 3$ [25] with μ_0 being the vacuum permeability and κ_0 being the spin-exchange enhancement factor due to the overlap of the alkali electron wave function and the nucleus of the noble gas [26]; $M = \mu \mathcal{N}$ corresponds to a fully polarized sample with atoms of magnetic moment μ and density $\mathcal{N}$.

As an aside, note that the transverse noble-gas nuclear spin damping rate, hence the comagnetometer bandwidth, is maximal if the applied longitudinal field matches [27]:

$$B_d = -B_n + B_e Q \frac{\gamma_n}{\gamma_e}, \qquad (7)$$

where $Q(P^e) = 4[2 - 4/(3 + P^{e\,2})]^{-1}$ is the electron slowing-down factor for ^{39}K [28]; γ_e and γ_n are the electronic and nuclear spin gyromagnetic ratios, respectively. This point is often referred to as the fast-damping field, which is better suited for high-bandwidth rotation measurements.

Under our experimental conditions, electronic spin magnetization B_e is small (~ 2 nT) compared to nuclear spin magnetization B_n (~ 100 nT) [9], leading to

$$B_c \approx B_d \approx -B_n = -\lambda M_n P^n. \qquad (8)$$

At this point, alkali spins are to first order insensitive to transverse magnetic fields but are still sensitive to nonmagnetic interactions [9].

B. Equilibrium condition

Suppose the comagnetometer has reached steady-state conditions for a given B_z, which is not the compensation point. Generally, if the device is brought to the compensation point by setting $B_z = B_c$, we will find that the system is no longer in equilibrium: the nuclear spin polarization will change over time. This can be seen, for instance, from the combination of Eqs. (2) and (3), which shows that the steady-state polarization depends on B_z (if the transverse gradient $\nabla B_\perp$ is not proportional to B_z). Consequently, B_c changes because $B_c \approx -B_n = -\lambda M_n P^n$, and the system is no longer at the compensation point.

If we wish to keep the system at the compensation point over an extended measurement time, it is possible to experimentally track it and lock the leading field such that $B_z = B_c$ [29,30]. In many cases, in closed-loop operation, however, the nuclear polarization will gradually decrease to zero, degrading the sensitivity of the comagnetometer.

It turns out that there exist special values of B_z where the system is in stable equilibrium at the compensation point. Here, the polarization does not change with time as the equilibrium polarization corresponds to the compensation point. From Eqs. (2), (3), and (8), one finds an equation for the leading field corresponding to the stationary system

$$B_z^2 + \lambda M_n P^e B_z + \frac{D_n}{R_{se}^{ne}} |\nabla B_\perp|^2 = 0. \qquad (9)$$

A solution for B_z exists only if

$$\left(\lambda M_n P^e\right)^2 - 4\frac{D_n}{R_{se}^{ne}} |\nabla B_\perp|^2 \geqslant 0, \qquad (10)$$

that is

$$\sqrt{\frac{R_{se}^{ne}}{4 D_n}} \lambda M_n P^e \geqslant |\nabla B_\perp|. \qquad (11)$$

This illustrates why high noble-gas pressures are desirable. Indeed, noting that the diffusion coefficient D_n is inversely proportional to $\mathcal{N}_n$, the magnitude of tolerable gradients scales as $\mathcal{N}_n^{3/2}$. Because P^e is limited to unity, and λ is a constant, the only ways to ensure the comagnetometer operates at the equilibrium compensation point are to use high nuclear spin density and/or more accurately zero the gradients.

In Fig. 1 one sees that, for a constant gradient $|\nabla B_\perp|$, the nuclear polarization, and hence the compensation field B_c, grows with external magnetic field B_z. In this figure, stationary compensation points can be found by looking for the intersection of the B_c curve with the diagonal (black dashed) line. In the case of $|\nabla B_\perp| = 0.5$ nT/cm (green solid line), these stationary points are indicated with orange and green stars. However, when $|\nabla B_\perp| = 1$ nT/cm (red solid line), no stationary compensation point exists.

In practice, part of the gradient may be related to the coils generating the leading field, therefore the field gradient may change with the B_z field. This effect is not included in the results presented in Fig. 1.

III. GRADIENT COMPENSATION

A. Experimental setup

The experimental setup is sketched in Fig. 2. We use a 20-mm-diameter spherical cell filled with 3 amg of ^{3}He and 50 torr of N_2. The cell has a sidearm loaded with a drop of alkali-metal mixture, 1% ^{87}Rb and 99% K molar
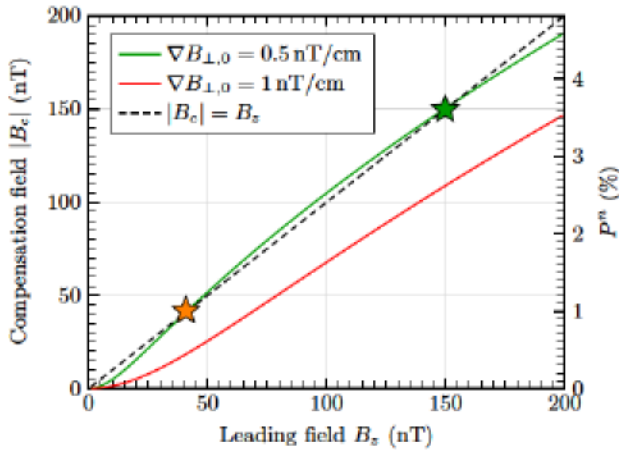
FIG. 1. Absolute value of the steady-state compensation field as a function of leading field B_z at high gradient (1 nT/cm, red solid line) and low gradient (0.5 nT/cm, green solid line). When the system is brought to such a field, it will generally self-adjust over time. However, the intersections of the green line with the dashed black line ($|B_c| = B_z$), marked with stars, correspond to equilibrium compensation points. Here, we make a distinction between the lower stationary compensation point (orange star) and the upper one (green star). These two points correspond to the roots of Eq. (9); however, the system is stable near the upper point and unstable near the lower one. In the simulation, the asphericity factor is $\alpha \mathcal{N}_n = 25$ nT/cm and the spin-exchange polarization rate is $R_{se}^{ne} = 4.5 \times 10^{-6}$ s^{-1}.
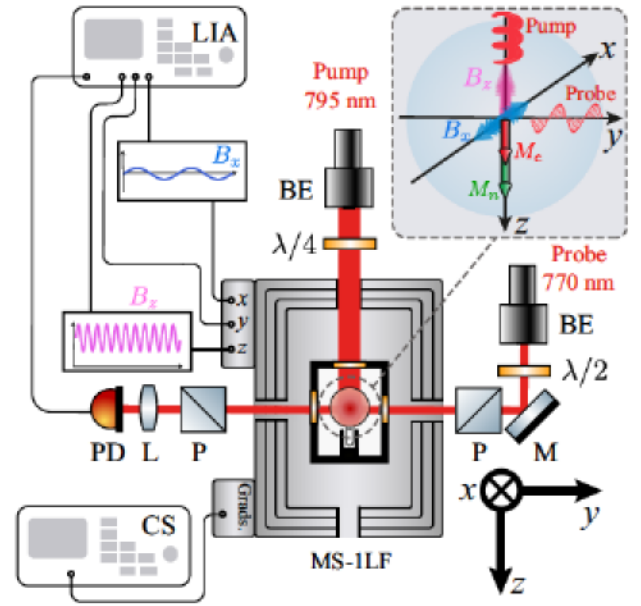

FIG. 2. Sketch of the experimental setup. LIA, lock-in amplifier; PD, photodetector; L, lens; CS, low-noise current source; P, polarizer; M, mirror; BE, beam expander; $\lambda/4$, quarter-wave plate; $\lambda/2$, half-wave plate; MS1-LF, magnetic shield. The inset shows the directions and polarizations of the laser beams; magnetic field modulations and the directions of the generated electronic and nuclear magnetization. The B_x modulation is only used for closed-loop control of the compensation point and ^{3}He magnetization measurement (see Sec. III B 2).

fractions. The vapor cell is placed in a Twinleaf MS-1LF magnetic shield. To minimize the effect of cell asphericity [3,31], the comagnetometer was mounted upright (z-axis along gravity) so that the cell sidearm is plugged by the liquid droplet of alkali metals. Note that other orientations of the stem are sometimes found to minimize the effects of asphericity [32]. Copper wires (not shown in Fig. 2) are looped around the cylindrical layers for degaussing of the shield and its content. We note that the cell was demagnetized with a commercial demagnetizer prior to being mounted in the oven. Self-magnetization of the cell, for example due to ferromagnetic impurities in the glass, is known to affect the usual quadratic dependence of T_1^n to B_z [see Eq. (3)]. In the presence of self- magnetization of the cell, T_1^n will be proportional B_z instead [33]. The working temperature of 185 °C is achieved with ac resistive heating. At this temperature, the ratio of Rb to K concentrations in the vapor is 3 : 97, which was measured by fitting the transmission spectrum of Rb D_2 and K D_1 lines.

Rubidium atoms are optically pumped by 70 mW of circularly polarized light from a Toptica TA Pro laser in resonance with the Rb D_1 line. For uniform pumping over the cell, the beam is expanded to 20-mm diameter. Potassium (and helium) spins are pumped by spin-exchange collisions with Rb. The comagnetometer readout is realized

by monitoring the polarization rotation of a linearly polarized probe beam (Toptica DL Pro) at about 16 mW/cm^2 (average intensity 7 mW and beam diameter 7.5 mm) detuned about 0.5 nm toward shorter wavelength from the K D_1 line. Because K atoms are pumped by spin-exchange optical pumping, the SERF magnetometer is much less sensitive to light shifts of the pump beam [7]. Both pump and probe beams are guided to the setup with optical fibers. No active stabilization of the lasers is performed apart from that of temperature and current of the diode lasers.

To perform low-noise detection of the response to perturbations along the y-axis, the B_z field is modulated with a sine wave (800 Hz, 35 nT peak to peak) [10,34] and the comagnetometer signal is analyzed with a lock-in amplifier. Details on the parametric modulation and chosen parameters are given in Appendix A 1. In typical SERF magnetometers, the lock-in detection is achieved by modulating the incident or output probe-beam polarization with photoelastic or Faraday modulators. Using magnetic field modulation instead is helpful to improve the compactness as well as lowering the cost, but the SERF resonance is then slightly broadened because of the modulation field (see Appendix A 1).

After zeroing the magnetic field in the cell and optimizing the pump and probe beam frequencies and powers, the

width of the SERF resonance was reduced to 8 nT, leading to a sensitivity to B_y field better than 10 fT/$\sqrt{\text{Hz}}$ at 20 Hz, limited by photon shot noise. This characterization was done prior to the gradient optimization and operating the system in the self-compensated regime.

B. Gradient optimization

From Eq. (3) one sees that the key to maximizing the nuclear polarization is reduction of transverse gradients

$$|\nabla B_\perp|^2 = (\partial_x B_x)^2 + (\partial_y B_x)^2 + (\partial_z B_x)^2$$
$$+ (\partial_x B_y)^2 + (\partial_y B_y)^2$$
$$+ (\partial_z B_y)^2. \qquad (12)$$

The Twinleaf MS-1LF magnetic shield provides five independent first-order gradient coils in a built-in flexible printed circuit board, allowing the shimming of the field gradient tensor. The procedure for zeroing transverse gradients involves two steps. The first step, as we will explain below (Sec. III B 1), is to use T_2^n as an indicator to zero the gradients of the longitudinal field B_z. Then, because $\nabla \times \boldsymbol{B} = 0$, the two T_1^n-relevant components appearing in Eq. (12), $\partial_x B_z = \partial_z B_x$ and $\partial_y B_z = \partial_z B_y$, are also nulled. The second step is to zero the other remaining independent components using the change of nuclear polarization as an indicator (see Sec. III B 2).

1. Optimization at low nuclear polarization

First, the gradients of the longitudinal field B_z are optimized away from the compensation point, at low nuclear polarization. The transverse decay rate of ^{3}He spins is known to be a function of the diffusion across z-field gradients [23],

$$\frac{1}{T_2^n} = \frac{8a^4 \gamma_n^2 |\nabla B_z|^2}{175 D_n}, \qquad (13)$$

where a is the cell radius and γ_n is the nuclear gyromagnetic ratio.

To accurately zero $|\nabla B_z|$, the following procedure is used. (i) Helium is polarized for 5 min with $B_z = 100$ nT. (ii) The B_y field is incremented by 5.5 nT to adiabatically tip the He spins away from the z-axis. (iii) After turning the B_y field off, the spins are left to precess. The precession is measured for 5 s by monitoring the probe beam before the pump beam is turned off (the weak probe beam is left on). Then the spins precess in the dark for 5 min before the pump beam is turned on to measure the precession signal again. The two precession amplitudes are compared to estimate T_2^n. (iv) Nuclear polarization is destroyed by applying a $\partial_z B_z$ gradient of the order of 30 nT/cm along the z-axis for 5 s. This is long enough to depolarize He
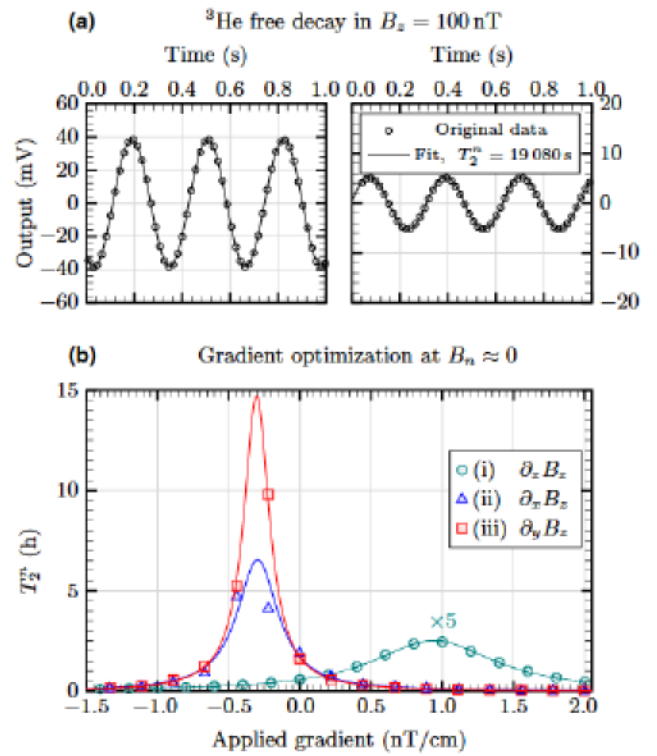

FIG. 3. Optimization of the transverse relaxation time of He nuclear spins at low polarization in a leading field of 100 nT. (a) Samples of ^{3}He free decay (left and right panels) separated by a dark time (pump laser off) of 37 660 s (about 10.5 h). Simultaneous fitting of the two data sets leads to $T_2^n = 19\,080(40)$ s (5.3 h). (b) Evolution of transverse relaxation time as a function of the B_z magnetic field gradients. The order of optimization is (i) $\partial_z B_z$, (ii) $\partial_x B_z$, (iii) $\partial_y B_z$. After a first round of gradient optimization, T_2^n increases from about 200 s to 15 h as suggested by the fits (solid lines) [see Eq. (13)].

spins (for details see Appendix A 2). The last step is important to make sure all measurements are realized at the same nuclear polarization.

The procedure is then repeated iteratively for different values of $\partial_i B_z$ gradients, in the sequence $i = z, x, y$. After each sequential step the respective gradient is set to its optimum value. The results are depicted in Fig. 3; the nuclear spin transverse relaxation time is seen to increase from about 200 s (no applied field gradients) to 15 h after a first round of optimization.

We note that this method is time-consuming not only because of the need to destroy ^{3}He polarization between measurements, but also because spins have to precess in the dark for some time for a precise measurement of T_2^n. This becomes increasingly problematic in the course of the optimization procedure as the transverse relaxation time increases. Each point in Fig. 3(b) necessitates about 10 min acquisition time.
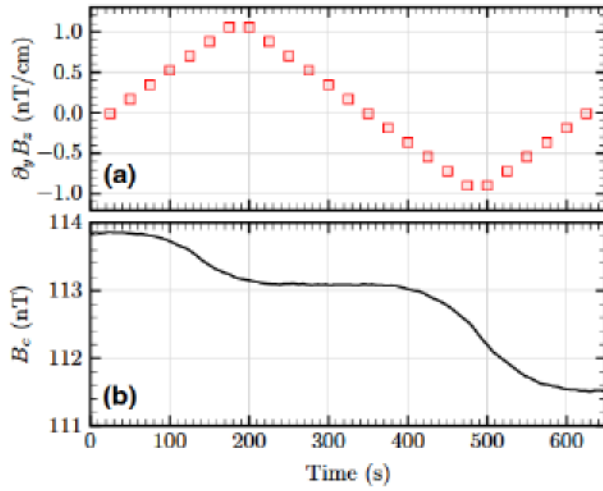
FIG. 4. Gradient-zeroing method at the compensation point. (a) Change of $\partial_y B_z$ gradient value as a function of time. (b) Effect of applied $\partial_y B_z$ gradient on the compensation field as a function of time.

2. Optimization at the compensation point

Once at the compensation point, we modulate the B_x field with a 40-Hz sine wave of about 0.1 nT amplitude [35]. The response of the comagnetometer with respect to B_z exhibits a dispersive resonance centered at $-B_n$ [8], which in our case is approximately equal to B_c [see Eq. (8)]. This resonance can be used for closed-loop control of the compensation point based on direct reference to the nuclear polarization which is an alternative to previous approaches locking to electronic resonance [29,30]. Our closed-loop control of the compensation field allows the comagnetometer always to be operated at optimum sensitivity, and the mechanisms affecting T_1^n or T_2^n can be studied in real time.

As coils intrinsically generate field gradients, it is important to be able to compensate for them at the working point. There are five independent first-order gradients; however, the optimization discussed in Sec. III B 1 only involves gradients of the longitudinal field. To maximize T_1^n, we use the following routine: we start by locking the field to the compensation point. We then vary one of the currents through the gradient coils over time: values are changed every 25 s following a sawtooth pattern [see Fig. 4(a)]. This way, the optimum gradient is sampled from different directions at different times, ensuring that effects of drifts are minimized. As a result of changing the gradient, the equilibrium nuclear polarization is changed, and so is the compensation point [see Fig. 4(b)], which is observed in real time with the closed-loop control.

Then each 25 s data set corresponding to a field gradient value is differentiated with respect to time in order to obtain the rate of change (in picotesla per second) of the compensation field as a function of the gradient value. The
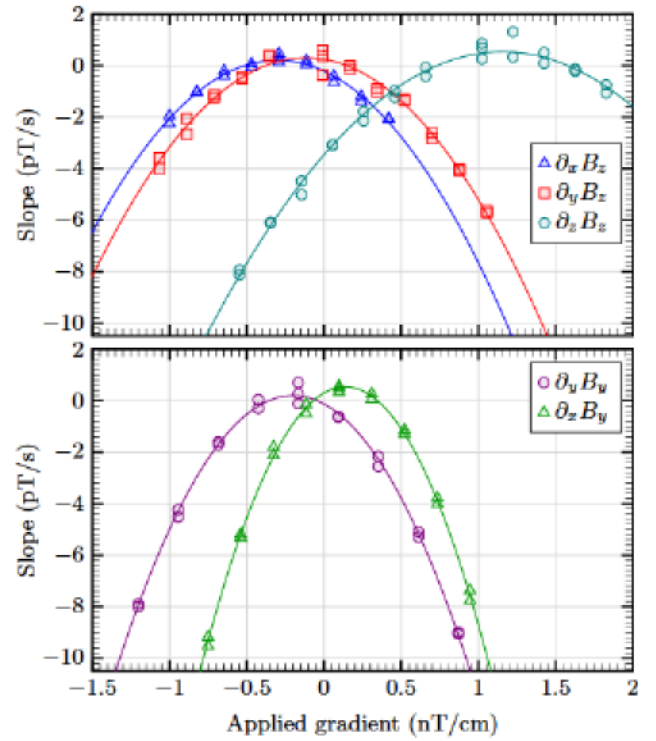

FIG. 5. Gradient optimization at the compensation point. The top panel shows the derivative of the time evolution of the compensation point as a function of the applied B_z gradients. The results for the other two independent gradient channels are shown in the bottom panel. The data are fitted with a parabola [see Eq. (3)], for which the center corresponds to the best compensated gradient. For discussions on the slope of parabolas (see the text and Table I).

results are depicted for each of the five independent gradient channels in Fig. 5. Fitting the slope as a function of applied gradient with a parabola (the derivation is given in Appendix B), the center, which corresponds to the best compensated gradient, is extracted. If the new center differs from the previous known value, we observe a buildup of the compensation field after moving to the new value, which indicates that a higher equilibrium field can be reached. This method has to be applied after large changes of the stationary compensation field (typically above 10 nT), since with different leading fields the gradients change as well. Note that this gradient optimization procedure works also when not at equilibrium nuclear polarization. Indeed, polarization buildup or decay linear in time does not affect the centers of the parabolas shown in Fig. 5. If the polarization changes in a nonlinear fashion, this is no longer the case. Thus, it is important to start with close-to-optimum values for the gradients, which can be obtained using the T_2^n method as discussed in Sec. III B 1.

Note that the magnetic field gradient generated by a gradient coil affects at least two gradient components. The actual gradient generated in our setup and the expected

TABLE I. Calculated and measured slope ratios of the parabolas for each independent magnetic gradient channel. The contribution of applied gradients to the slope is calculated using Eq. (12), and compared to that of the $\partial_x B_z$ channel. Each "coil" label refers to the principal component of the generated gradient. Note that, for a given channel, other gradients are also generated with similar or smaller coefficients. The complete set of applied transverse gradients for each channel is listed in the second column. The coefficients depend on the coil windings and are provided by the shield manufacturer.

Coil	Applied $\nabla B_\perp$ gradient	Calc. ratio	Meas. ratio
$\partial_x B_y$	$\partial_x B_y + \partial_y B_x + 0.34\, \partial_y B_y$	2.17	2.68(11)
$\partial_y B_y$	$\partial_y B_y - 0.68\, \partial_x B_x$	1.46	1.75(7)
$\partial_x B_z$	$\partial_z B_x$	1	1
$\partial_y B_z$	$\partial_z B_y$	1	0.95(5)
$\partial_z B_z$	$-0.5\, \partial_x B_x - 0.5\, \partial_y B_y$	0.5	0.64(3)

slope of parabolas in Fig. 5 are summarized in Table I. Our results show that, as predicted, the $\partial_x B_y$ gradient is of greatest concern, while the $\partial_z B_z$ has about four times less impact. However, a sizable deviation between expected and measured ratios is also observed. We attribute this error to not well-known calibration factors and coefficients of the gradient coils. Indeed, estimates are provided by the gradient coil manufacturer, obtained by simulating the generated field in the absence of the magnetic shield. This suggests our method for gradient optimization could also be used for *in-situ* calibration of gradient coils which we plan to investigate further.

IV. POLARIZATION DYNAMICS

In Fig. 6, we use the experimental method presented in Ref. [8] to show how gradients affect the dynamics of spin-exchange optical pumping of ^{3}He nuclear spins for a leading field of 150 nT and an electronic polarization of about 50%. The electronic polarization is chosen to optimize the sensitivity of the comagnetometer, while the nuclear polarization is determined by the requirement of operation at a stable compensation point [see Eq. (11)]. When the gradients are uncompensated the steady-state nuclear field reaches 115 nT. When the gradients are exaggerated (reversal of all optimized gradients) the steady-state value drops to 70 nT. No stationary compensation point could be found for either of these configurations. When the gradients are fully optimized, the nuclear field reaches above $B_n \approx 140$ nT (corresponding to a nuclear polarization of about 3%) [36]. In this regime a stable compensation point exists. It was found at 131 nT, determined by the conditions described by Eq. (11). Note this is slightly below the maximum polarization of 140 nT achieved with a leading field of 150 nT displayed in Fig. 6. At this compensation field, a noise level corresponding to a sensitivity to nuclear spin-dependent energy shifts of approximately 3×10^{-22} eV$/\sqrt{\text{Hz}}$ was achieved in the
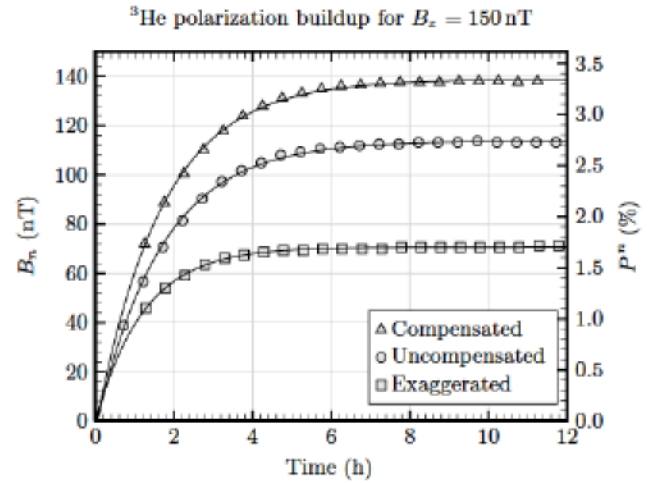

FIG. 6. Dynamics of spin-exchange optical pumping of ^{3}He nuclear spins in a leading field of 150 nT. The circles were obtained when there were no applied gradients. The squares were obtained when the gradients were exaggerated by changing the sign of the optimized applied gradients (triangles). Each data set was fitted (solid lines) assuming an exponential approach of the nuclear field to the equilibrium value over time [see Eq. (1)].

range 0.1–1 Hz. In terms of gyroscopic sensitivity, this corresponds to about 0.5 μrad s$^{-1}/\sqrt{\text{Hz}}$ (≈ 80 nHz$/\sqrt{\text{Hz}}$), which is 2.5 fT$/\sqrt{\text{Hz}}$ in terms of pseudo-magnetic field sensitivity. To estimate the sensitivity of the system we measured the spectrum of the output signal and calibrated it with a routine based on magnetic field modulation adapted from Ref. [37].

Once the system's parameters are determined, different strategies can be employed to reach the stable stationary compensation point starting from an unpolarized system. The nuclear polarization dynamics for different strategies are illustrated by numerical simulations displayed in Fig. 7. Three strategies are considered.

(i) the leading field is set to the upper stable compensation field value and the optical pumping rate is adjusted to have maximum sensitivity of the comagnetometer, corresponding to $P_e \approx 0.5$.

(ii) The leading field is set to a value much larger than the upper stable compensation field (in our conditions 400 nT, practically limited by, for example, the coil current source) together with a higher optical pumping rate, such that $P_e \approx 1$, until the upper stationary compensation field is reached. Then the leading field can be locked and the optical pumping rate adjusted such that the system has the highest sensitivity [the conditions of strategy (i)].

(iii) The parameters are set to strategy (ii) until the polarization passes the lower stationary compensation point, after which the parameters are set to strategy (i). In this case, the system's nuclear polarization field will continue
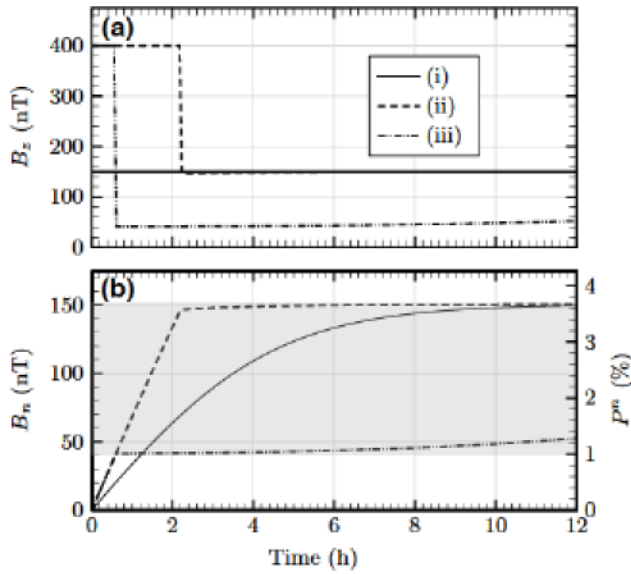
FIG. 7. Calculated dynamics of three nuclear polarization strategies. (a) Applied magnetic field as a function of time. (b) Dynamics of the nuclear polarization. Calculations are made with parameters similar to that in Fig. 1 and $|\nabla B_\perp| = 0.5$ nT. The gray shaded area shows the nuclear field in between the two stationary compensation points, located at $B_n = 40$ nT and $B_n = 150$ nT (see also Fig. 1). When the nuclear field is in this area, the closed-loop control of the compensation point can be turned on to allow the nuclear field to move to the highest compensation point over time. Strategy (i) involves applying a z-field equal to the known upper stationary compensation field, $B_n = 150$ nT. Strategies (ii) and (iii) involve applying, at $t = 0$, a larger field than in (i) (here, 400 nT) and a higher pumping rate (such that $P_e = 1$) during the initial stage. Closed-loop control of the compensation field can be turned-on either when reaching the upper stationary compensation field [strategy (ii)] or right after passing over the lower one [$B_n = 40$ nT, strategy (iii)].

to grow until it reaches the upper stationary compensation field.

The benefit of the latter strategy is that the comagnetometer is operational in the fastest time, for the given simulation parameters, within 35 mins. This could be beneficial, for example, for gyroscopic applications on board vehicles. The changing nuclear polarization while employing strategy (iii) affects the signal-to-noise ratio of the gyroscope, but the device remains operational in the process. Our simulations show, however, that with this strategy, it takes about 50 h for the system to reach steady-state nuclear polarization. Strategy (ii) is a good alternative to have the system quickly operational at the upper stationary compensation point, i.e. at steady-state nuclear polarization.

V. CONCLUSION

Motivated by applications in NMR-based rotation sensing, searches for ultralight bosonic dark matter, and experiments measuring exotic spin-dependent interactions, we constructed a dual-species (K-^{3}He) comagnetometer with hybrid optical pumping (via Rb atoms) operating in self-compensating regime.

Building on the body of earlier work by several groups, we developed a method for closed-loop control of the compensation point allowing practical optimization of the operating parameters in spite of the inherently slow (hours to days) dynamics of the system. When the comagnetometer operates at the compensation point, it is generally insensitive to magnetic fields. However, we showed that the system can still be optimized in terms of magnetic gradients and fields without changing the operation mode.

The gradient optimization method presented facilitates achieving much higher longitudinal and transverse relaxation times than are otherwise possible, improving the polarization level and stability. At the compensation point, this also increases the coupling between the nuclear and electronic spins and improves stability of the compensation point. With these, our method has potential to boost the performance of comagnetometer nuclear-spin-ensemble-based quantum memory [17–19], amplifiers [38–41], and gyroscopes [11,29,42].

Finally, the device shows a sensitivity comparable to the best previous comagnetometers [14], but at a several times smaller density of ^{3}He. The helium number density of 3 amg used in this work is lower than in most previous studies. Since lower-pressure cells are easier to manufacture and safer to operate, the optimization technique allows for wide usability of vapor-cell-based nuclear spin sensors in various application areas.

APPENDIX A: MEASUREMENT DETAILS

1. SERF magnetometer

We measured the polarization of K via Faraday rotation of a linearly polarized probe beam. The rotation magnitude is in proportional to the component of K polarization P_y^e according to [21]

$$\theta = \frac{1}{2} n_e r_e c D f_{D_1} \frac{\nu - \nu_{D_1}}{(\nu - \nu_{D_1})^2 + \left[\Gamma_{\text{tot}}^{D_1}/(2\pi)\right]^2} P_y^e, \quad \text{(A1)}$$

where $n_e = 7.5 \times 10^{13}$ cm^{-3} is the number density of K, $r_e = 2.8 \times 10^{-15}$ m is the classical electron radius, $c = 3 \times 10^8$ m/s is the speed of light, $D = 2$ cm is the cell diameter, $f_{D_1} = 1/3$ is the oscillator strength for the D_1 transition at frequency $\nu_{D_1} = 389.236$ THz, $\nu = 389.539$ THz is the laser frequency, and $\Gamma^{D_1}_{tot}/(2\pi) = 48$ GHz is the half-width at half-maximum of the transition. With these values, the maximum rotation angle, corresponding to $P^e_y = 1$, is 0.7 rad.

An optical polarimeter was used to read out the rotation angle as shown in Fig. 2, and the decrossing angle between two polarizers was set to $\pi/4$. Thus, the signal $I \propto \sin^2(\theta - \pi/4) \approx 0.5 - \theta$ is linearly dependent on the rotation angle.

To suppress low-frequency drifts, we applied a modulation field $B^m_z \sin(\omega_m t)$ along the pumping axis (see, for example, Ref. [43]). Consequently, P^e_y is a sum of harmonics. Under the assumption that the field component B_z is small, the approximate solution to the first harmonic is [10,34]

$$P^e_y(\omega_m) = -\frac{2 P^e_z R_{tot} \gamma_e Q}{Q^2 R^2_{tot} + (\gamma_e B_y)^2} J_0\left(\frac{\gamma_e B^m_z}{Q\omega_m}\right)$$
$$\times J_1\left(\frac{\gamma_e B^m_z}{Q\omega_m}\right) B_y \sin(\omega_m t), \quad \text{(A2)}$$

where the $J_i(\cdot)$ are Bessel functions of the first kind of order i, Q is the slowing-down factor, and R_{tot} is the total relaxation rate of K. For a modulation frequency of 800 Hz and $Q = 5.2$ (assuming $P^e = 50\%$), the factor $J_0(\gamma_e B_m/Q\omega_m) J_1(\gamma_e B^m_z/Q\omega_m)$ is maximized for $B^m_z = 161$ nT. However, when B^m_z is large, the modulation field causes rf broadening of magnetic resonance transitions, and the relaxation rate is given by [14]

$$R_{rf} = \frac{5}{36} \frac{(\gamma_e B^m_z)^2}{Q^2 R_{se}}, \quad \text{(A3)}$$

where $R_{se} = n_e \sigma_{ee} v = 79\,000$ s^{-1} is the alkali-alkali spin-exchange rate with the collision cross section $\sigma_{ee} = 1.5 \times 10^{-14}$ cm^2. For $B^m_z = 161$ nT, the rate is $R_{rf} = 52$ s^{-1}, being five times larger than the spin destruction ratio of K on He. We experimentally found that the sensitivity of the K magnetometer peaks at $B^m_z = 35$ nT, which balances the beneficial effect of larger B^m_z on the signal amplitude with its deleterious effect on the linewidth due to the rf broadening. The signal was fed into a lock-in amplifier and demodulated at the first-harmonic to retrieve the rotation angle.

To suppress the alkali polarization gradient, we employ a hybrid pumping technique where an optically thin sample of Rb atoms is optically pumped and the K atoms are polarized via spin-exchange collisions with the Rb atoms.

Uniform optical pumping can be achieved with a high ratio of the receiver to donor densities.

In general, both K and Rb can be the spin donor. Because of the high He pressure in our cell, the spin destruction collisions between alkali atoms and He atoms are the dominant source of relaxation. Given that the spin-destruction cross section of K on He is around 18 times smaller than that of Rb on He [26,44], we chose K as the receiver in the hope of achieving a better magnetometer sensitivity.

Note that the modulation of B_x or B_y fields also results in a usable magnetic resonance. However, in that case the projection of the electronic spins on the z-axis is then modulated periodically too, leading to a lower average electronic spin polarization along the z-axis and therefore a lower equilibrium nuclear polarization, in turn affecting the stability of the comagnetometer [Eq. (11)].

2. Depolarization of nuclear spins with applied gradients

In Sec. III B 1 we proposed a method to optimize the gradients at low nuclear polarization. To make sure all the measurements are performed at the same nuclear polarization, step (iv) consists of destroying nuclear polarization by applying a 30 nT/cm $\partial_z B_z$ gradient for 5 s. It should be stressed that by implementing this step, one needs to make sure that nuclear polarization is completely destroyed. One parameter to consider in this context is the diffusion rate between slices in which the rotation angle of the spins changes by π. The thickness of such a slice is

$$\delta z = \frac{1}{2\gamma_n \nabla B_z \delta t}, \quad \text{(A4)}$$

where $\gamma_n = 3.24 \times 10^{-2}$ Hz/nT is the gyromagnetic ratio of ^{3}He nuclear spins, ∇B_z is the applied z-gradient and δt is the time it is applied. With $\nabla B_z = 30$ nT/cm and $\delta t = 5$ s, we find $\delta z = 0.11$ cm. Noting that, for our experimental conditions, $D_{^3He} \approx 0.71$ cm^2/s, ^{3}He spins diffuse through multiple slices during step (iv), which leads to depolarization. Note that, during step (ii), the nuclear magnetization was rotated in the y-z plane. Besides, applying a $\partial_z B_z$ gradient automatically generates a $\partial_y B_y$ gradient, contributing together to the depolarization of longitudinal and transverse nuclear spins [Eqs. (3) and (13)].

APPENDIX B: TIME DERIVATIVE OF POLARIZATION IN GRADIENT OPTIMIZATION PROCESS

The solution of Eq. (1) gives the time evolution of the nuclear polarization as

$$P^n(t) = P^n_s + [P^n(0) - P^n_s]$$
$$\times \left\{1 - \exp\left[-(R^{ne}_{se} + 1/T^n_1)t\right]\right\}, \quad \text{(B1)}$$

where $P^n(0)$ is an initial value of the polarization and P_s^n is the steady-state polarization defined in Eq. (2) by $P^n(t \to \infty)$. Therefore, the time derivative of the nuclear polarization is

$$\frac{d}{dt}P^n(t) = \left[R_{se}^{ne} + 1/T_1^n\right]\left[P_s^n - P^n(0)\right]$$
$$\times \exp\left[-(R_{se}^{ne} + 1/T_1^n)t\right]. \quad (B2)$$

In our experiment, the measurement period for a given gradient value lasts for 25 s, which is much shorter than T_1^n, therefore we can approximate $\exp(-t/T_1^n) \approx 1$. In addition, $\exp(-R_{se}^{ne}t) \approx 1$ since $R_{se}^{ne} \lesssim 1/T_1^n$. Moreover, throughout the whole zeroing procedure the initial polarization for each measurement varies by less than 5%, therefore for simplicity we assume it to be constant over all measurements within the zeroing procedure. This leads to the following equation for the time derivative of the polarization in each measurement

$$\frac{d}{dt}P^n(t) = (R_{se}^{ne} + 1/T_1^n)(P_s^n - P^n(0)). \quad (B3)$$

Then, using Eqs. (2) and (3), one can get an expression for the polarization time derivative as a function of the gradients of transversal fields $|\nabla B_\perp|$ (see Fig. 5):

$$\frac{d}{dt}P^n(t) = R_{se}^{ne}[P^e - P^n(0)] - \frac{D_n}{B_z^2}P^n(0)|\nabla B_\perp(t)|^2, \quad (B4)$$

where the time dependence of the gradient is due to the change in its value during the zeroing routine.

---

[1] J. Kitching, S. Knappe, and E. A. Donley, Atomic sensors – a review, IEEE Sens. J. **11**, 1749 (2011).

[2] J. Kitching, Chip-scale atomic devices, Appl. Phys. Rev. **5**, 031302 (2018).

[3] T. W. Kornack and M. V. Romalis, Dynamics of Two Overlapping Spin Ensembles Interacting by Spin Exchange, Phys. Rev. Lett. **89**, 253002 (2002).

[4] W. Happer and A. C. Tam, Effect of rapid spin exchange on the magnetic-resonance spectrum of alkali vapors, Phys. Rev. A **16**, 1877 (1977).

[5] J. C. Allred, R. N. Lyman, T. W. Kornack, and M. V. Romalis, High-Sensitivity Atomic Magnetometer Unaffected by Spin-Exchange Relaxation, Phys. Rev. Lett. **89**, 130801 (2002).

[6] M. Padniuk, M. Kopciuch, R. Cipolletti, A. Wickenbrock, D. Budker, and S. Pustelny, Response of atomic spin-based sensors to magnetic and nonmagnetic perturbations, Sci. Rep. **12**, 324 (2022).

[7] M. V. Romalis, Hybrid Optical Pumping of Optically Dense Alkali-Metal Vapor without Quenching Gas, Phys. Rev. Lett. **105**, 243001 (2010).

[8] Y. Lu, Y. Zhai, W. Fan, Y. Zhang, L. Xing, L. Jiang, and W. Quan, Nuclear magnetic field measurement of the spin-exchange optically pumped noble gas in a self-compensated atomic comagnetometer, Opt. Express **28**, 17683 (2020).

[9] T. W. Kornack, R. K. Ghosh, and M. V. Romalis, Nuclear Spin Gyroscope Based on an Atomic Comagnetometer, Phys. Rev. Lett. **95**, 230801 (2005).

[10] L. Jiang, W. Quan, R. Li, W. Fan, F. Liu, J. Qin, S. Wan, and J. Fang, A parametrically modulated dual-axis atomic spin gyroscope, Appl. Phys. Lett. **112**, 054103 (2018).

[11] J. Liu, L. Jiang, Y. Liang, G. Li, Z. Cai, Z. Wu, and W. Quan, Dynamics of a Spin-Exchange Relaxation-Free Comagnetometer for Rotation Sensing, Phys. Rev. Appl. **17**, 014030 (2022).

[12] Y. Liang, L. Jiang, J. Liu, W. Fan, W. Zhang, S. Fan, W. Quan, and J. Fang, Biaxial Signal Decoupling Method for the Longitudinal Magnetic-Field-Modulated Spin-Exchange-Relaxation-Free Comagnetometer in Inertial Rotation Measurement, Phys. Rev. Appl. **17**, 024004 (2022).

[13] K. Wei, T. Zhao, X. Fang, Z. Xu, C. Liu, Q. Cao, A. Wickenbrock, Y. Hu, W. Ji, J. Fang, and D. Budker, Ultrasensitive Atomic Comagnetometer with Enhanced Nuclear Spin Coherence, Phys. Rev. Lett. **130**, 063201 (2023).

[14] G. Vasilakis, J. M. Brown, T. W. Kornack, and M. V. Romalis, Limits on New Long Range Nuclear Spin-Dependent Forces Set with a K-^{3}He Comagnetometer, Phys. Rev. Lett. **103**, 261801 (2009).

[15] W. A. Terrano and M. V. Romalis, Comagnetometer probes of dark matter and new physics, Quantum Sci. Technol. **7**, 014001 (2021).

[16] I. M. Bloch, Y. Hochberg, E. Kuflik, and T. Volansky, Axion-like relics: New constraints from old comagnetometer data, J. High Energy Phys. **2020**, 167 (2020).

[17] O. Katz, R. Shaham, and O. Firstenberg, Quantum Interface for Noble-Gas Spins Based on Spin-Exchange Collisions, PRX Quantum **3**, 010305 (2022).

[18] R. Shaham, O. Katz, and O. Firstenberg, Strong coupling of alkali-metal spins to noble-gas spins with an hour-long coherence time, Nat. Phys. **18**, 506 (2022).

[19] O. Katz, R. Shaham, E. Reches, A. V. Gorshkov, and O. Firstenberg, Optical quantum memory for noble-gas spins based on spin-exchange collisions, Phys. Rev. A **105**, 042606 (2022).

[20] In our work, the nuclear polarization in the self-compensated regime was above 3%. For comparison, the nuclear polarization in Ref. [14] was comparable, but with four times the noble gas density.

[21] V. Shah and M. V. Romalis, Spin-exchange relaxation-free magnetometry using elliptically polarized light, Phys. Rev. A **80**, 013416 (2009).

[22] L. D. Schearer and G. K. Walters, Nuclear spin-lattice relaxation in the presence of magnetic-field gradients, Phys. Rev. **139**, A1398 (1965).

[23] G. D. Cates, S. R. Schaefer, and W. Happer, Relaxation of spins due to field inhomogeneities in gaseous samples at low magnetic fields and low pressures, Phys. Rev. A **37**, 2877 (1988).

[24] R. Barbé, M. Leduc, and F. Laloë, Résonance magnétique en champ de radiofréquence inhomogène - 2e partie: Vérifications expérimentales; mesure du coefficient de self-diffusion de 3He, J. Phys. **35**, 935 (1974).

[25] In cgs units, $\lambda = 8\pi\kappa_0/3$.

[26] A. Ben-Amar Baranga, S. Appelt, M. V. Romalis, C. J. Erickson, A. R. Young, G. D. Cates, and W. Happer, Polarization of ^{3}He by Spin Exchange with Optically Pumped Rb and K Vapors, Phys. Rev. Lett. **80**, 2801 (1998).

[27] J. Lee, Ph.D. thesis, Princeton University, 2019.

[28] I. M. Savukov and M. V. Romalis, Effects of spin-exchange collisions in a high-density alkali-metal vapor in low magnetic fields, Phys. Rev. A **71**, 023405 (2005).

[29] L. Jiang, W. Quan, F. Liu, W. Fan, L. Xing, L. Duan, W. Liu, and J. Fang, Closed-Loop Control of Compensation Point in the K-Rb-^{21}Ne Comagnetometer, Phys. Rev. Appl. **12**, 024017 (2019).

[30] C. Tang, C. Liu, C. A. G. Prado, T. Zhao, B. Han, and Y. Zhai, Design of real time magnetic field compensation system based on fuzzy PI control algorithm for comagnetometer, J. Phys. D: Appl. Phys. **55**, 355106 (2022).

[31] M. V. Romalis, D. Sheng, B. Saam, and T. G. Walker, Comment on "new limit on Lorentz-Invariance- and *CPT*-Violating Neutron Spin Interactions Using a Free-Spin-Precession ^{3}He-^{129}Xe Comagnetometer", Phys. Rev. Lett. **113**, 188901 (2014).

[32] W. A. Terrano, J. Meinel, N. Sachdeva, T. E. Chupp, S. Degenkolb, P. Fierlinger, F. Kuchler, and J. T. Singh, Frequency shifts in noble-gas comagnetometers, Phys. Rev. A **100**, 012502 (2019).

[33] J. M. Brown, *A new Limit on Lorentz-And CPT-Violating Neutron Spin Interactions Using a Potassium-Helium Comagnetometer* (Princeton University, 2011), p. 147.

[34] Z. Li, R. T. Wakai, and T. G. Walker, Parametric modulation of an atomic magnetometer, Appl. Phys. Lett. **89**, 134105 (2006).

[35] The modulation frequency should be higher than the Larmor frequency of ^{3}He, while not being too far away to obtain a reasonable sensitivity.

[36] Higher nuclear spin polarization can be achieved, for example 30% in Ref. [18]. However, this was done at 100% electronic polarization and at a higher leading field. Therefore, the 30% polarization is not at the stable compensation point. The polarization in our experiment is similar to that in Ref. [14].

[37] T. Kornack, Ph.D. thesis, Princeton University, 2005.

[38] M. Jiang, H. Su, A. Garcon, X. Peng, and D. Budker, Search for axion-like dark matter with spin-based amplifiers, Nat. Phys. **17**, 1402 (2021).

[39] M. Jiang, Y. Qin, X. Wang, Y. Wang, H. Su, X. Peng, and D. Budker, Floquet Spin Amplification, Phys. Rev. Lett. **128**, 233201 (2022).

[40] Y. Wang, H. Su, M. Jiang, Y. Huang, Y. Qin, C. Guo, Z. Wang, D. Hu, W. Ji, P. Fadeev, X. Peng, and D. Budker, Limits on Axions and Axionlike Particles within the Axion Window Using a Spin-Based Amplifier, Phys. Rev. Lett. **129**, 051801 (2022).

[41] Y. Wang, Y. Huang, C. Guo, M. Jiang, X. Kang, H. Su, Y. Qin, W. Ji, D. Hu, and X. Peng *et al.*, Sapphire: Search for exotic parity-violation interactions with quantum spin amplifiers, arXiv preprint arXiv:2205.07222 (2022).

[42] L. Jiang, J. Liu, Y. Liang, M. Tian, and W. Quan, A single-beam dual-axis atomic spin comagnetometer for rotation sensing, Appl. Phys. Lett. **120**, 074101 (2022).

[43] P. Put, P. Wcisło, W. Gawlik, and S. Pustelny, Nonlinear magneto-optical rotation with parametric resonance, Phys. Rev. A **100**, 043838 (2019).

[44] T. G. Walker, I. A. Nelson, and S. Kadlecek, Method for deducing anisotropic spin-exchange rates, Phys. Rev. A **81**, 032709 (2010).